Int. J. Electrochem. Sci., 14 **(2019)** 4496 – 4507, doi: 10.20964/2019.05.63

International Journal of
ELECTROCHEMICAL
SCIENCE
www.electrochemsci.org

Nano-wrinkle MnO_2 film Prepared by Anodic Deposition for Pseudocapacitor applications

Wei Yan, Kai Zhuo, Jianlong Ji, Qiang Zhang and Shengbo Sang[*]

Micro-Nano System Research Center, Key Lab of Advanced Transducers and Intelligent Control System of the Ministry of Education & College of Information and Computer, Taiyuan University of Technology, Taiyuan 030024, China.
[*]E-mail: sunboa-sang@tyut.edu.cn

Received: 9 February 2019 / *Accepted:* 10 March 2019 / *Published:* 10 April 2019

Nano-wrinkle MnO_2 films were facilely deposited on the Ni foam substrate with the method of anodic deposition. The morphology and structure of MnO_2 films were investigated by the aid of field-emission scanning electron microscopy(FE-SEM), energy-dispersive spectrometer and X-ray diffraction. The images of FE-SEM showed that the deposited MnO_2 films comprised of spherical granules with the nano-wrinkle structure. Nano-wrinkle surface provided a larger specific surface area for better contact of the active material with the electrolyte. The thickness of the MnO_2 film was controlled easily by changing the electrodeposition time. The pseudocapacitive characters of the nano-wrinkle MnO_2 electrodes were illustrated by cyclic voltammetry, charge-discharge and electrochemical impedance spectroscopy. Nano-wrinkle MnO_2 films presented specific capacitance of $327.4F \cdot g^{-1}$ at the current density of $0.1A \cdot g^{-1}$, and the capacitance retention remained at 70.0% of its maximum after 7500 cycles even at the current density of $10A \cdot g^{-1}$ in charge-discharge processes.

Keywords: Pseudocapacitor, MnO_2 films, Nano-wrinkle, Electrodeposition

1. INTRODUCTION

With the increasingly rising expectations in the field of the clean, safe and renewable energy, supercapacitors (SCs) have attracted much attention as a device for efficient energy storage [1]. Supercapacitors have been widely used in modern electronics due to their high power density, distinguished cycle performance and high-speed charge-discharge [2, 3]. Based on the employment of electrode materials, SCs are generally classified into electric double-layer capacitors (EDLC), pseudocapacitors and hybrid supercapacitors which integrate the EDLC and pseudocapacitors.

The EDLC is based on the charge separation at the interface between electrode and electrolyte, which is primarily concentrated on carbon-based materials [4, 5]. The pseudocapacitors rely on the redox

reaction occurring in the electrode [6]. However, supercapacitors are exclusively employed together with batteries due to poor energy density is a common drawback in practical application [7]. In order to obtain high specific capacitance and energy density of supercapacitors, transition metal oxides/hydroxides are brought into sharp focus as active materials [8, 9]. Among these materials, oxides of transition metal have been developed as electrode materials for the pseudocapacitors such as MnO_2[10-12], NiO [13], Co_3O_4 [14], RuO_2 [15] and V_2O_5 [16]. Recently, manganese oxide (MnO_2) is considered as a promising electrode materials for pseudocapacitor due to its high theoretical specific capacitance ($1370F \cdot g^{-1}$), low price and environmental compatibility [17, 18]. Nevertheless, poor electrical conductivity of MnO_2 and structural instability has impeded its electrochemical property in practical application. To attain high specific capacitance, one simple way is to synthesize nano-structural MnO_2 films on conductive substrates to form the binder-free electrodes. Furthermore, this kind of the binder-free electrode is able to receive enhancement of the electrical conductivity and effective utilization of the active materials, thus contributing to rapid electron transfer between MnO_2 and conductive substrate, high capacitance and high rate capability [19].

So far, a large number of synthetic routes have been developed to prepare MnO_2, for instance, electrodeposition technique [20], hydrothermal synthesis [21] and sol-gel synthesis [22]. Among these methods, the electrodeposition approach has been used owing to its merits such as facility and free binder [23]. Depending on the differences of deposition potential/current, the electrodeposition of MnO_2 is separated to different branches as potentiostatic (PS), galvanostatic (GS), cyclic voltammetric and pulse eletrodeposition techniques [24]. These different modes have a significant influence on the morphology and the structure of MnO_2 film, which are also resulted in the pseudocapacitive performance. In potentiostatic mode, the deposition occurs continuously under a constant voltage with few byproducts.

In this paper, the MnO_2 electrode was deposited on nickel foam with the anode potentiostatic method, which is able to increase the contact area between active materials and solutions by electrodeposition on nickel foam. In addition, the insertion/extraction of electrolyte ions and electrons into the electrode material structure can be accelerated, thereby developing the actual capacitance value and the rate performance of the capacitance.

2. MATERIAL AND METHODS

2.1. Materials

$Mn(CH_3COO)_2$, CH_3COONa, Na_2SO_4, nickel foam (PPI 110, $250g \cdot m^{-3}$~$280g \cdot m^{-3}$, 0.5mm thick, Kunshan long San Bao Electronic Material Co., Ltd., China). All of these chemicals are analytically pure and can be adopted for this work.

2.2. Electrodeposition of MnO_2

The Ni foams (size: 1cm×2cm) were ultrasonically cleaned in ethanol and distilled water for 10 minutes in sequence. Then an insulating paint was applied to control electrodeposition area(1cm×1cm)

of Ni foam. The MnO_2 film was electrodeposited in a three-electrode system based on a CS2350H electrochemical workstation (Wuhan Corrtest Instruments Corp., China). The counter electrode and reference electrode were Ni foam and Ag/AgCl, respectively. The Ni foam was used as the working electrode and the conductive substrate. The electrolyte was an aqueous solution consisting of 0.05M $Mn(CH_3COO)_2$ and 0.1M CH_3COONa. Electrodeposition experiments were in progressed at constant potential modes of 1.1V, 1.3V, 1.5V, 1.7V versus Ag/AgCl electrode for 1min, corresponding samples were abbreviated as S1, S2, S3 and S4. The samples of the deposition time at 1.1V varied by 5min and 9min, which were expressed as S5 and S6, respectively. Detailed conditions and specific capacitance at $1A \cdot g^{-1}$ for all samples were listed in Table 1. The as-prepared electrodes were rinsed for three times by distilled water and dried at the room temperature. Furthermore, the weight of MnO_2 was measured by comparing the mass of the nickel foam before and after the deposition.

Table 1. Preparation conditions and specific capacitance of as-prepared electrodes

Sample	Deposition potential (V)	Deposition time (min)	Mass of deposition (mg)	Specific capacitance ($F \cdot g^{-1}$)
S1	1.1	1	0.32	141.4
S2	1.3	1	0.48	129.8
S3	1.5	1	0.53	105.6
S4	1.7	1	0.44	117.0
S5	1.1	5	2.29	82.6
S6	1.1	9	3.17	70.5

2.3 Characterization

Field-emission scanning electron microscopy (FE-SEM, Japan, Hitachi) and energy-dispersive spectrometer (EDS) were operated at 10kV. The X-ray diffraction (XRD, Rigaku D/Max-3B, Japan) with Cu-Ka of 1.5404Å was adopted to characterize the structure of the as-scraped off manganese oxide powder at the scanning rate of 2 degree/min.

2.4 Electrochemical measurements

The electrochemical properties of the pseudocapacitor electrodes were explored in a three-electrode configuration system on the basis of a CS2350H electrochemical workstation (Wuhan Corrtest Instruments Corp., Ltd, China), which was driven by the CS Studio5 software. Besides, all electrochemical tests were performed at the room temperature in the aqueous solution containing of 1M Na_2SO_4. Meanwhile, the as-prepared MnO_2 electrodes were used as the working electrode, while a Pt foil (1cm×2cm) and an Ag/AgCl electrode were used as the counter electrode and the reference electrode, respectively. On the other hand, the electrochemical performance of the MnO_2 electrodes was evaluated by cyclic voltammetry (CV), charge-discharge and electrochemical impedance spectroscopy (EIS).

Specifically, CV tests were conducted within the potential range of 0V~1V with the scan rates ranging from $10mV \cdot s^{-1}$ to $100mV \cdot s^{-1}$. Charge-discharge was performed within the potential range of 0V~0.8V with the current densities ranging from $0.1A \cdot g^{-1}$ to $10A \cdot g^{-1}$. EIS was analyzed within the frequency range of 0.1Hz ~100kHz.

The specific capacitance value of the electrode system was evaluated based on the CV curves under the following Eq. (1) [25]:

$$C_{CV} = \int IdV / (2m\nu\Delta V) \quad (1)$$

where I (A) is the applied current, ΔV is the tested potential range, ν($V \cdot g^{-1}$) is the scan rate, and m (g) is the mass of the MnO_2 film.

The average specific capacitance of the electrode system consists of electrodeposited MnO_2, which was also measured according to the charge-discharge data obtained from charge-discharge curves under the following Eq. (2):

$$C_{CD} = i\Delta t / m\Delta V \quad (2)$$

Where i (A) is the discharging current, and Δt(s) is the discharging time.

3. RESULTS AND DISCUSSION

3.1. Structural and morphological characterization

The FE-SEM images and the corresponding EDS profiles of the as-prepared MnO_2 films were shown in Fig. 1. As shown, MnO_2 was uniformly deposited over the framework of the Ni foam substrate respectively at 1.1V, 1.3V, 1.5V and 1.7V; meanwhile, the thin film was formed. Fig. 1(c) showed the MnO_2 film displayed spherical granules with a nano-wrinkle structure, indicating the film served as an uneven material allowing the electrolyte ions to diffuse easily through the electrode body, resulting in an increase in the number of redox reactions occurring in the electrochemical process. When increasing the deposition time, the thickness of MnO_2 film would rise significantly, as shown in Fig. 2(a-c). From Fig. 2(a-c), the surface structure of the MnO_2 films were much smoother with a longer deposition time. Moreover, the corresponding EDS profiles (Fig. 2(d)) confirmed the presence of Mn and O in the as-deposited film, whose atomic ratio was close to 1:2, further indicating the composition of MnO_2.

Fig. 3 showed the XRD patterns of the sample after the thermal annealing, which indicated the formation of γ-MnO_2. Diffraction peaks (23.45, 36.76, 65.98) correspond to the crystal planes (110), (021) and (061) assigned to nano-wrinkle structure. Although the intensity was relatively low and the crystallinity was relatively weak, the prepared product can be confirmed as γ-MnO_2, except for the diffraction peaks of Ni substrate [26, 27].

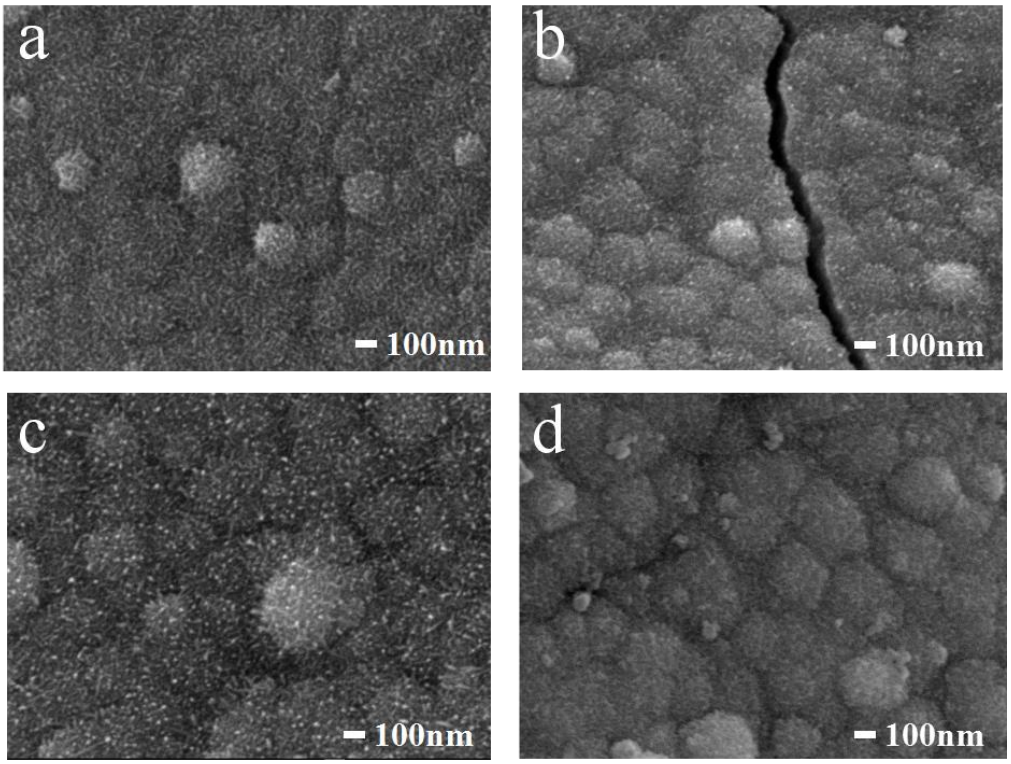

Figure 1. (a-d) FE-SEM images of MnO_2 deposited at 1.1V, 1.3V, 1.5V and 1.7V for 1min.

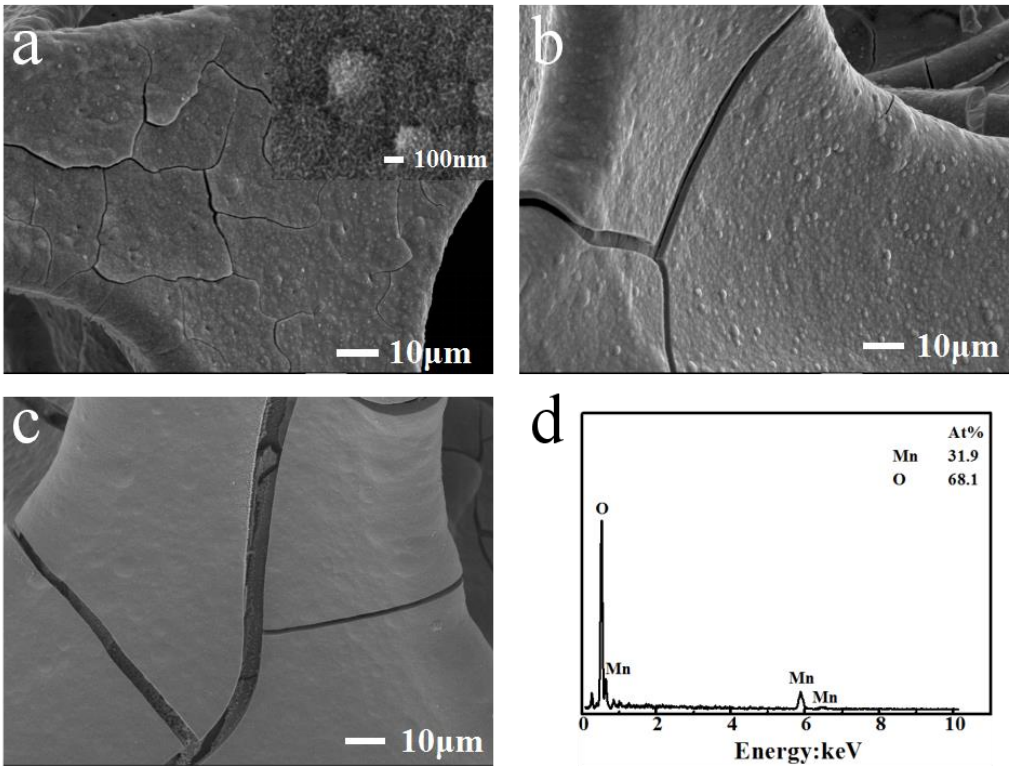

Figure 2. (a-c) FE-SEM images of MnO_2 deposited on Ni foam at 1.1V for 1min, 5min and 9 min, and (d) the corresponding EDS profiles of MnO_2 films deposited at 1.1V for 1min.

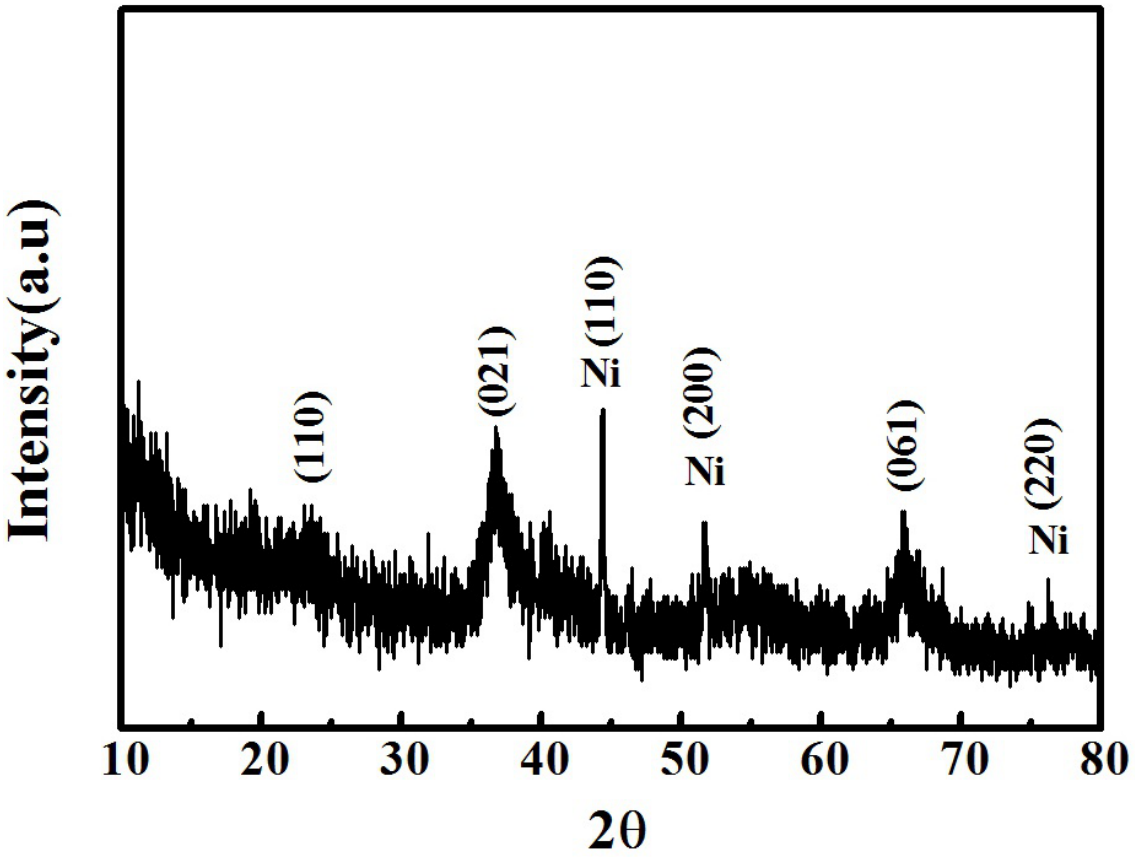

Figure 3. XRD patterns of the films containing γ-MnO_2 nanoflakes electrodeposited on the Ni foam by potentiostatic.

3.2. Electrochemical tests in 1M Na_2SO_4 electrolyte

Capacitive performance of the materials obtained was evaluated by cyclic voltammetry (CV), charge-discharge as well as electrochemical impedance spectroscopy (EIS). Additionally, the as-prepared MnO_2 films with nano-wrinkle structure was directly used as the working electrode.

CV, charge-discharge and EIS analyzations were adopted to estimate the electrochemical performance of the as-prepared MnO_2 electrode materials. Fig. 4(a) showed CV curves of MnO_2 films, with S1, S2, S3 and S4 electrodes in a potential window of 0V to 1V at the scan rate of $10mV \cdot s^{-1}$. The pure nickel foam showed non-pseudocapacitance, as the peak current just reached less than 0.2mA, thus the contribution to the capacitance was negligibly small. These non-rectangular ones verified the pseudocapacitive nature of the MnO_2 electrodes. Simultaneously, the charge-discharge of the electrode took place at the constant rate of CV. The rectangular shape of the voltammograms further manifested the ideal capacitating behavior of the materials. As shown in Fig. 4(b), the S1 electrode achieved a high specific capacitance of $189.3F \cdot g^{-1}$ at the scan rate of $10mV \cdot s^{-1}$. In contrast, the S2, S3 and S4 electrodes presented the capacitance values of $98.8F \cdot g^{-1}$, $103.1F \cdot g^{-1}$ and $156.5F \cdot g^{-1}$ at the same scan rate. With the increase of the current density, C_{CV} declined and reached $108.2F \cdot g^{-1}$ at the scan rate of $100mV \cdot s^{-1}$. The S1 electrode displayed a maximum spot in CV curve, resulting in a splendid electrochemical performance. Fig. 4(c) showed typical charge-discharge curves of MnO_2 electrode deposited at different potentials for 1min at $1A \cdot g^{-1}$. The specific capacitance of the four electrodes was respectively $141.4F \cdot g^{-}$

^{1}, 129.8F·g^{-1}, 105.6F·g^{-1} and 117.0F·g^{-1} at 1A·g^{-1}, which was consistent with the CV results, further demonstrating the ideal capacitive characteristic and speedy charge-discharge property of the MnO_2 electrode.

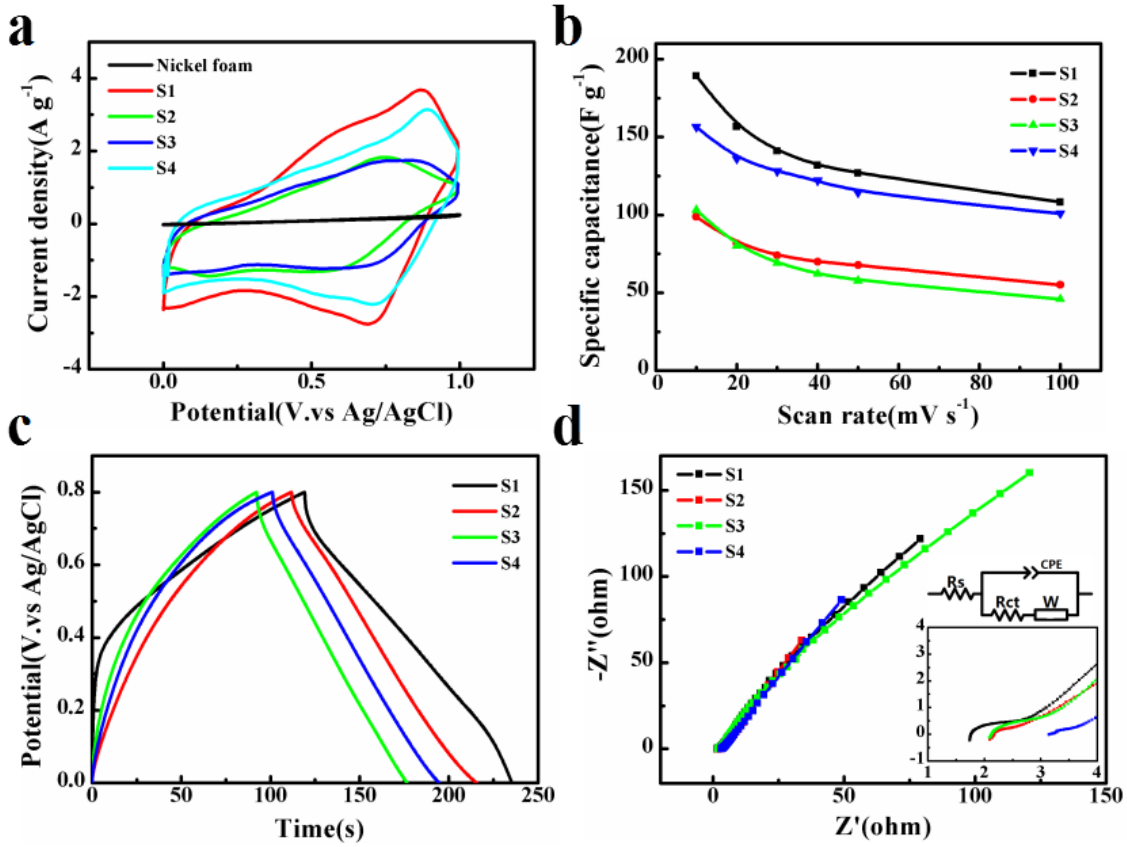

Figure 4. Electrochemical performance of MnO_2 deposited at different potentials for 1min: (a) Comparison of CV curves at 10mV·s^{-1} and (b) Specific capacitance at different scan rates; (c) Charge-discharge profiles at 1A·g^{-1} and (d) Nyquist plot.

Fig. 5(a) demonstrated the CV curves of the MnO_2 film deposited at 1.1V respectively for 1mins, 5mins and 9mins. These three types of electrodes represented the pseudocapacitive characteristics from the shape of redox peaks. According to Fig. 5(b), the specific capacitance of S5 and S6 electrodes synthesized at different time was respectively 135.2F·g^{-1} and 100.4F·g^{-1} at the scan rate of 10mV·s^{-1}. Fig. 5(c) showed the charge-discharge curves of the MnO_2 electrode prepared at different electrodeposition time. Similar to Fig. 4(c), Fig. 5(c) presented a symmetrical and closely linear slope during the charge-discharge procedures, which indicated a superior pseudocapacitive behavior. Based on Eq. (2), the specific capacitance of S5 and S6 electrodes was 82.6F·g^{-1} and 70.5F·g^{-1} at 1A·g^{-1}, respectively.

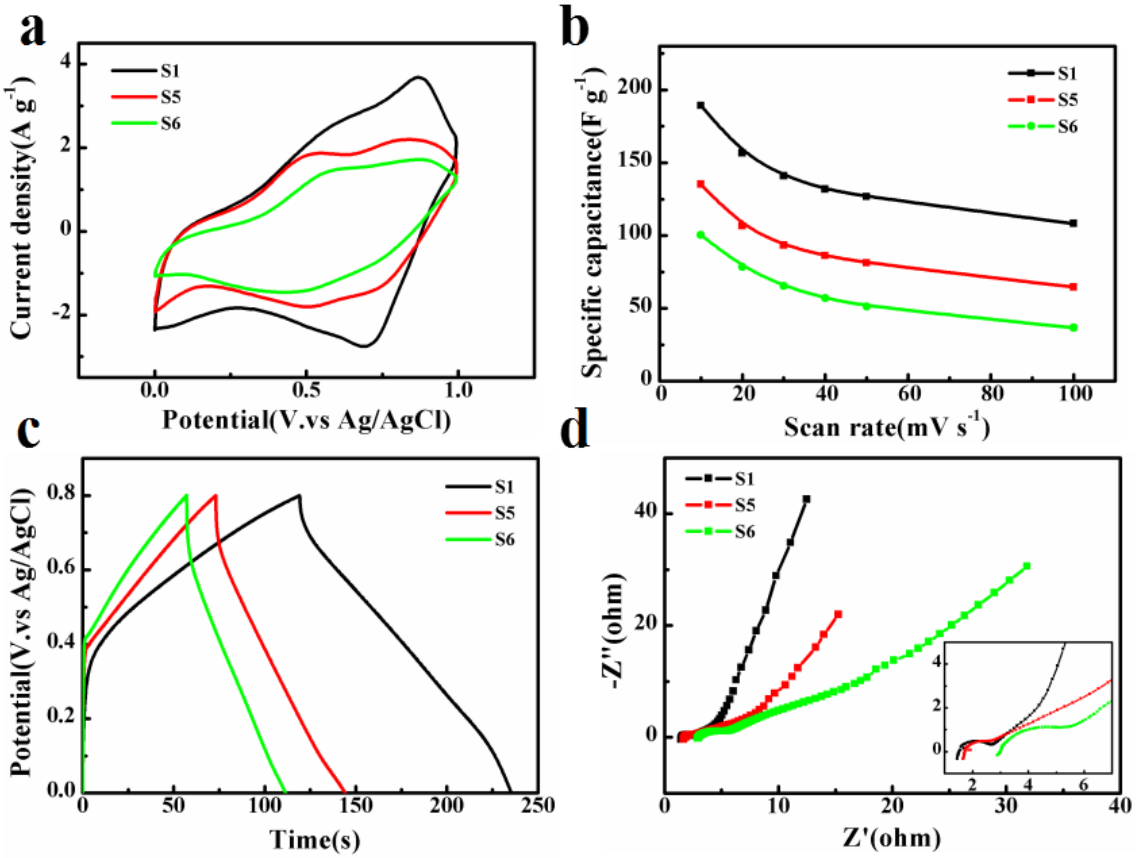

Figure 5. Electrochemical performance of MnO_2 deposited at 1.1V at different eletrodeposition time: (a) Comparison of CV curves at 10mV·s^{-1} and (b) Specific capacitance at different scan rates; (c) Charge-discharge profiles at 1A·g^{-1} and (d) Nyquist plot.

In order to show the supercapacitive properties of the S1 electrode, CV curves were utilized at different scan rates including 10mV·s^{-1}, 20mV·s^{-1}, 30mV·s^{-1}, 40mV·s^{-1}, 50mV·s^{-1} and 100mV·s^{-1} within a fixed potential range of 0V~1.0V versus Ag/AgCl, whose corresponding CV results were shown in Fig. 6(a). The CV information displayed curves of similar rectangle at different scan rates with a distinct oxidation peak. It is indicating an ideal pseudocapacitive behavior caused by the reversible and sequence redox reactions of the MnO_2 film surface in short time involving adsorption of cation in electrolyte(i.e. Na^+ and H^+ incorporation) as described in Eq. (3) [28, 29].

$$MnO_2 + xNa^+ + yH^+ + (x+y)e^- \leftrightarrow MnOONa_xH_y \qquad (3)$$

As shown in Fig. 6(b), the charge-discharge curves of S1 electrode with different current densities (0.1A·g^{-1}, 0.2A·g^{-1}, 0.5A·g^{-1}, 1A·g^{-1}, 2A·g^{-1}, 5A·g^{-1}, 10A·g^{-1}) potentially ranged from 0V to 0.8V. The characteristics of the charge-discharge curves indicated a redox behavior, as shown in the CV curves (Fig. 6(a)). According to the discharge time, the specific capacitance of S1 electrode was calculated by Eq. (2), which were respectively obtained at 327.4F·g^{-1}, 227.3F·g^{-1}, 162.7F·g^{-1}, 120.7F·g^{-1}, 80.4F·g^{-1}, 39.3F·g^{-1} and 23.0A·g^{-1} under the current densities of 0.1A·g^{-1}~10A·g^{-1}. A comparison of the electrochemical features of MnO_2 obtained under different current densities showed that an increase in the current density from 0.1A·g^{-1} to 10A·g^{-1} would lead to a decrease in specific capacitance.

Additionally, the inspected capacitance values were also comparable with other reported for nanostructural MnO_2 prepared with the electrodeposition approaches so far (e.g. 2790mF·cm^{-2} at the current density of 2mA·cm^{-2} for mesoporous MnO_2 nanosheets by cyclic voltammetric [19], 383F·g^{-1} at the current density 2mA·cm^{-2} for NF-MnO_2 by potentiodynamic electrodeposition [30], 235.5F·g^{-1} at the scan rate of 25mV·s^{-1} for MnO_2 nanobelts by Pulse base-electrogeneration [31], 242F·g^{-1} at the current density of 2A·g^{-1} for MnO_2 nanorods by pulse electrodeposition [32], 0.59F·cm^{-2} at the current density of 5mA·cm^{-2} for CNT/MnO_2 electrode prepared by virtue of the galvanostatic electrodeposition modes [33],)

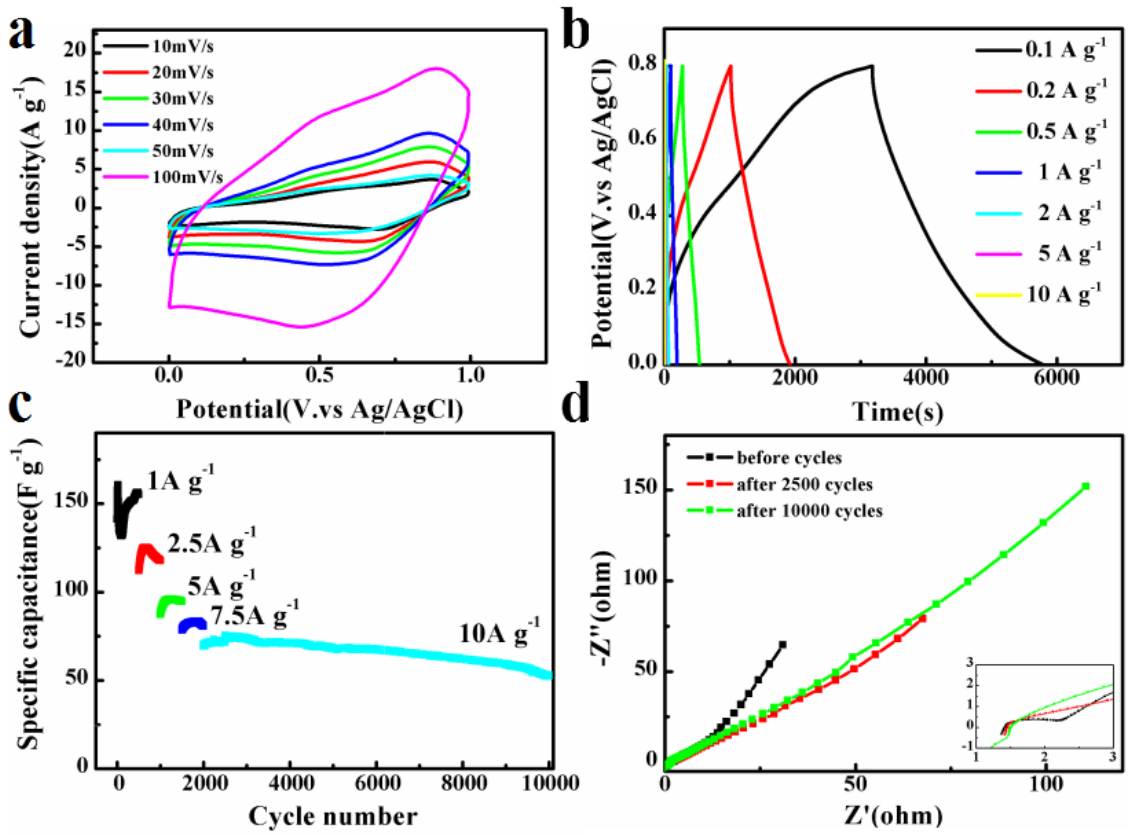

Figure 6. Electrochemical performance of MnO_2 deposited at 1.1V for 1min: (a) CV curves at different scan rates from 10mV·s^{-1} s to 100mV·s^{-1} and (b) Charge-discharge curves at different current densities (0.1 A·g^{-1}, 0.2 A·g^{-1}, 0.5 A·g^{-1}, 1A·g^{-1}, 2A·g^{-1}, 5A·g^{-1}, 10A·g^{-1}); (c) Cycling performance of MnO_2 deposited at 1.1V for 1min at different current densities and (d) Nyquist plot within the frequency range of 0.1 Hz ~100 kHz.

Further EIS was carried out on the prepared MnO_2 electrodes within the frequency range of 0.1Hz~100kHz amplitude of 10mV at an open circuit potential. The equivalent circuit was shown as insert section in Fig. 4(d), which was composed of a solution resistance (R_s), a charge-transfer resistance (R_{ct}), a constant phase element (CPE) and the Warburg impedance [34]. All Nyquist diagrams showed a straight line in the low-frequency area and a small half circle in the high-frequency area, which resembled an ideal pseudocapacitor behavior. The high-frequency at the real impedance part (Z′) at the

start of the half circle represented the equivalent series resistance (ESR),which was to measure the total ionic resistance of the electrolyte, the inherent resistance of the electrodes [35].

Fig. 4(d) and 5(d) showed the Nyquist plots of the MnO_2 electrodes obtained at different potentials of different periods of time. The electrode materials investigated was possessed of the following values of Rs: 1.6Ω (S1), 2.1Ω (S2), 2.1Ω (S3), 3.2Ω (S4), 1.8Ω (S5) and 3.0Ω (S6). The high value of R_s was attributed to the low conductivity of MnO_2 and production of MnO_x in the process of deposition. Fig. 5(d) showed that the R_{ct} of the sample was 1.1Ω, 0.4Ω, and 2.3Ω, respectively. It is indicated that the amount of active material interfered with the charge-transfer process. Besides, the oblique line in the low frequency region became gentler with the increase of deposition time, further indicating the low conductivity of the material and the hindrance to ion dispersion. Moreover, the conductivity of the MnO_2 electrode deposited at 1.1V for 1min exhibited relatively low impedance, thus further confirming the superiority of the electrode.

The cyclic performance of the MnO_2 electrode was measured at a 0-0.8V potential window in Fig. 6(c). During the first 100 cycles at current density of $1A \cdot g^{-1}$,the specific capacitance of the MnO_2 electrode decreased sharp from to $160F \cdot g^{-1}$ to $132F \cdot g^{-1}$ that may be limited by ion transfer and activity of MnO_2. Approximately, the specific capacitors presented an upward trend in 500 cycles at current density of $1A \cdot g^{-1}$, $2.5A \cdot g^{-1}$, $5A \cdot g^{-1}$, $7.5A \cdot g^{-1}$. The specific capacitance of the electrode rose to the maximum and then fell due to changes and shedding in the active materials. At the current density of $10A \cdot g^{-1}$, the specific capacitance reached $75.4F \cdot g^{-1}$ and corresponding capacitance retention of the electrode reached 70.0% after 7500 cycles, which can be considered that the active material was detached from the electrode during the charge-discharge process.

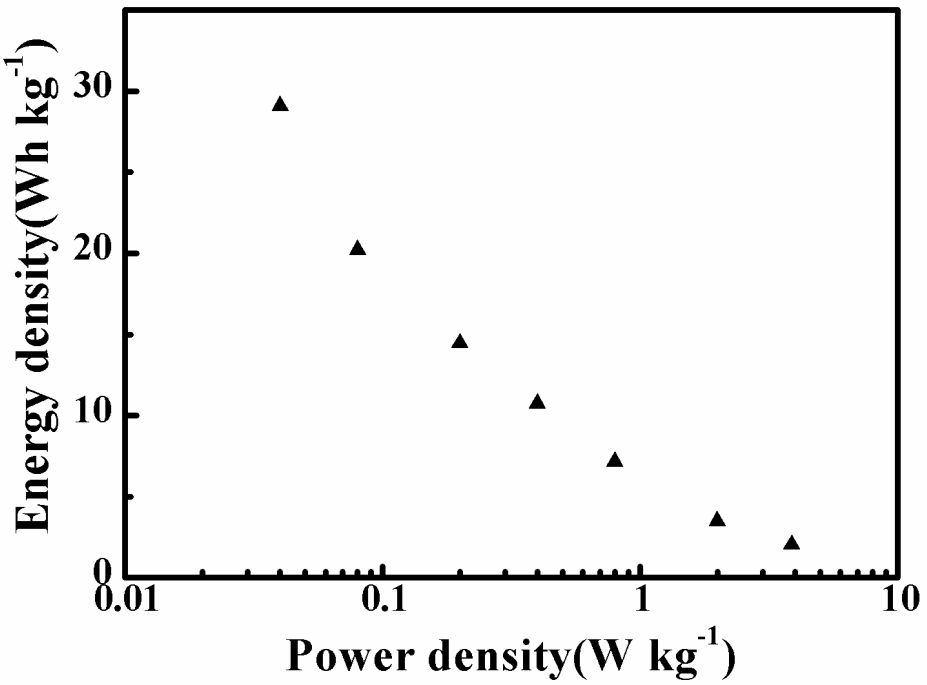

Figure 7. Ragone plot of the MnO_2 electrode deposited at 1.1V for 1min.

The power density of pseudocapacitors was closely related to ESR[36]. The energy and power densities of the MnO_2 electrode were plotted together based on the data reported in a previous publication in Fig. 7. Besides, the power density ($kW \cdot kg^{-1}$) and energy density ($Wh \cdot kg^{-1}$) were calculated using the following formulas [37]:

$$E = C(\Delta V)^2 / 7.2 \quad (4)$$

$$P = 3.6E / \Delta t \quad (5)$$

Where C is the specific capacitance ($F \cdot g^{-1}$), ΔV is the supercapacitor potential range (V), and Δt is the discharging time (s). It was found that the MnO_2 deposited at 1.1V for 1min presented the energy density of 29.1$Wh \cdot kg^{-1}$ at the power density of 0.04 $kW \cdot kg^{-1}$.

4. CONCLUSIONS

In summary, the nano-wrinkle MnO_2 films were electrodeposited on Ni foam applied a cost-effective one-step electrodeposition approach for fabricating a high-performance electrode of pseudocapacitor. The thickness of the MnO_2 film was controlled easily by changing the electrodeposition time. The nano-wrinkle MnO_2 electrode deposited at 1.1V for 1min exhibited a high specific capacity of 327.4$F \cdot g^{-1}$ and the considerable energy density of 29.1$Wh \cdot kg^{-1}$ at the current density of 0.1$A \cdot g^{-1}$. Furthermore, the capacitance remained above 70.0% of its maximum value after 7500 cycles even at the current density of 10$A \cdot g^{-1}$. Therefore, the nano-wrinkle MnO_2 film can be considered as a promising candidate for high energy storage of pseudocapacitor.

ACKNOWLEDGEMENT
This study was supported by National Natural Science Foundation of China (No.51622507, No.51705354, No.61703298).

References

1. L. Abbasi, M. Arvand, *Appl. Surf. Sci,* 445 (2018) 272.
2. T.A. Babkova, H. Fei, N.E. Kazantseva, I.Y. Sapurina, P. Saha, *Electrochim. Acta*, 272 (2018) 1.
3. V.D. Nithya, N.S. Arul, *J. Power Sources*, 327 (2016) 297.
4. T. Wanchaem, S. Rattanamai, P. Dulyaseree, P. Khanchaitit, W. Wongwiriyapan, *Materials Today Proceedings,* 4 (2017) 6620.
5. S. Lehtimäki, S. Tuukkanen, J. Pörhönen, P. Moilanen, J. Virtanen, M. Honkanen, D. Lupo, *Appl. Phys. A*, 117 (2014) 1329.
6. L. Liu, *J. Power Sources*, 239 (2013) 24.
7. T. Zhu, Z. He, G. Zhang, Y. Lu, C. Lin, Y. Chen, H. Guo, *Journal of Alloys & Compounds*, 644 (2015) 186.
8. A. Eftekhari, M. Mohamedi, *Materials today energy*, 6 (2017) 211.
9. M. Huang, L. Wang, S. Chen, L. Kang, Z. Lei, F. Shi, H. Xu, Z.H. Liu, *Rsc Advances* 7 (2017) 10092.
10. X. Cui, X. Chen, W. Zhang, X. Yan, M. Wang, J. Lian, Z. Zheng, H. Deng, *Journal of Alloys & Compounds*, 695 (2017) 2109.

11. F. Liao, X. Han, Y. Zhang, C. Xu, H. Chen, *Ceram. Int*., 44 (2018): 22622.
12. F. Liao, X. Han, D. Cheng, Y. Zhang, X. Han, C. Xu, H. Chen, *Ceram. Int.*, 45 (2019): 1058.
13. Y. Zheng, Y. Li, J. Yao, Y. Huang, S. Xiao, *Ceram. Int*., 44 (2018) 2568.
14. H. Zhang, Y. Zhou, Y. Ma, J. Yao, X. Li, Y. Sun, Z. Xiong, D. Li, *Journal of Alloys & Compounds*, 740 (2018) 174.
15. Y. Chang, W. Zhou, J. Wu, G. Ye, Q. Zhou, D. Li, D. Zhu, T. Li, G. Nie, Y. Du, *Electrochim. Acta*, 283 (2018) 744.
16. H. Li, J. He, X. Cao, L. Kang, X. He, H. Xu, F. Shi, R. Jiang, Z. Lei, Z.H. Liu, *J. Power Sources*, 371 (2017) 18.
17. W. Yang, Q. Chen, X. Song, H. Tan, H. Liu, *Ceram. Int*., 44 (2018) 13858.
18. J. Qin, Z.-S. Wu, F. Zhou, Y. Dong, H. Xiao, S. Zheng, S. Wang, X. Shi, H. Huang, C. Sun, X. Bao, *Chin. Chem. Lett.*, 29 (2018) 582.
19. J. Yang, L. Lian, H. Ruan, F. Xie, M. Wei, *Electrochim. Acta,* 136 (2014) 189.
20. E.K. Kim, N.K. Shrestha, W. Lee, G. Cai, S.H. Han, *Materials Chemistry & Physics*, 155 (2015) 211.
21. J. Chu, D. Lu, J. Ma, M. Wang, X. Wang, S. Xiong, *Mater. Lett.,* 193 (2017) 263.
22. W. Tang, X. Shan, S. Li, H. Liu, X. Wu, Y. Chen, *Mater. Lett.*, 132 (2014) 317.
23. S.L. Chou, J.Z. Wang, S.Y. Chew, H.K. Liu, S.X. Dou, *Electrochem. Commun*., 10 (2008) 1724.
24. S. Rodrigues, A.K. Shukla, N. Munichandraiah, *J. Appl. Electrochem*., 28 (1998) 1235.
25. R. Rajagopal, K.S. Ryu, *Electrochim. Acta,* 265 (2018) 532.
26. S. Chou, F. Cheng, J. Chen, *J. Power Sources*, 162 (2006) 727.
27. Y. Chabre, J. Pannetier, *Progress in Solid State Chemistry*, 23 (1995) 0.
28. M. Kundu, L. Liu, *J. Power Sources*, 243 (2013) 676.
29. L.-K. Wu, J. Xia, G.-Y. Hou, H.-Z. Cao, Y.-P. Tang, G.-Q. Zheng, *Electrochimica Acta*, 191 (2016) 375.
30. P.R. Jadhav, M.P. Suryawanshi, D.S. Dalavi, D.S. Patil, E.A. Jo, S.S. Kolekar, A.A. Wali, M.M. Karanjkar, J.H. Kim, P.S. Patil, *Electrochim. Acta*, 176 (2015) 523.
31. M. Aghazadeh, M.G. Maragheh, M.R. Ganjali, P. Norouzi, F. Faridbod, *Appl. Surf. Sci.*, 364 (2016) 141.
32. L. Lin, S. Tang, S. Zhao, X. Peng, N. Hu, *Electrochimica Acta*, 228 (2017) 175.
33. Mirzaee, Majid, C. Dehghanian , K. S. Bokati, *Applied Surface Science*, 436 (2017) 1050.
34. M. Aghazadeh, M. Asadi, M.G. Maragheh, M.R. Ganjali, P. Norouzi, F. Faridbod, *Appl. Surf. Sci*., 364 (2016) 726.
35. M. Kazazi, *Ceram. Int*. 44 (2018) 10863.
36. M. Mirzaee, C. Dehghanian, K. Sabet Bokati, *Appl. Surf. Sci.*, 436 (2018) 1050.
37. P.R. Deshmukh, Y. Sohn, W.G. Shin, *Electrochim. Acta*, 285 (2018) 381.